LANGMUIR

pubs.acs.org/Langmuir Article

Mechanistic Insights into Interactions at Urea−Hydroxyapatite Nanoparticle Interface

Nimshi L. Fernando, Dhanusha T. N. Rathnayake, Nilwala Kottegoda, J. K. D. Sumedha Jayanetti, Veranja Karunaratne, and Dilushan R. Jayasundara*

Cite This: https://doi.org/10.1021/acs.langmuir.1c00564 Read Online

ACCESS | Metrics & More | Article Recommendations | Supporting Information

ABSTRACT: Development of controlled release biomolecules by surface modification of hydroxyapatite nanoparticles has recently gained popularity in the areas of bionanotechnology and nanomedicine. However, optimization of these biomolecules for applications such as drug delivery, nutrient delivery requires a systematic understanding of binding mechanisms and interfacial kinetics at the molecular level between the nanomatrix and the active compound. In this research, urea is used as a model molecule to investigate its interactions with two morphologically different thin films of hydroxyapatite nanoparticles. These thin films were fabricated on quartz crystal piezoelectric sensors to selectively expose Ca^{2+} and PO_4^{3-} sites of hydroxyapatite. Respective urea adsorption and desorption on both of these sites were monitored *in situ* and in real time in the phosphate buffer solution that mimics body fluids. The measured kinetic parameters, which corroborate structural predisposition for controlled release, show desorption rates that are one-tenth of the adsorption rates on both surfaces. Furthermore, the rate of desorption from the PO_4^{3-} site is one-half the rate of desorption from the Ca^{2+} site. The Hill kinetic model was found to satisfactorily fit data, which explains cooperative binding between the hydroxyapatite nanoparticle thin film and urea. Fourier transform infrared spectra and X-ray photoemission spectra of the urea adsorbed on the above surfaces confirm the cooperative binding. It also elucidates the different binding mechanisms between urea and hydroxyapatite that contribute to the changes in the interfacial kinetics. These findings provide valuable information for structurally optimizing hydroxyapatite nanoparticle surfaces to control interfacial kinetics for applications in bionanotechnology and nanomedicine.

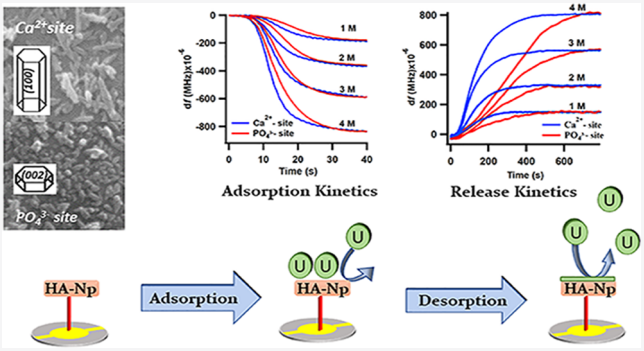

Downloaded via Dilushan Jayasundara on May 21, 2021 at 13:50:59 (UTC).
See https://pubs.acs.org/sharingguidelines for options on how to legitimately share published articles.

■ INTRODUCTION

Development of novel and sustainable drug and fertilizer storage/release systems have received high scientific focus in recent times. These novel systems contain numerous advantages such as enhanced bioavailability, controlled and prolonged release, greater efficacy, and safety.[1−3] Moreover, the development of controlled release nanohybrids by encapsulating biomolecules into hydroxyapatite nanoparticles (HA-Nps) have recently gained popularity. HA-Nps are considered as promising candidates in medicinal applications due to their bioactivity and biocompatibility.[4−16] As a rich source of phosphorus, HA-Nps are also used in the field of agriculture.[17−23] Furthermore, hydroxyapatite surface offers rich opportunities for the immobilization of strategic chemicals through systematic surface modification.[6,24−27] However, the impact of surface morphology of HA-Nps on the encapsulation/release mechanism of these biomolecules remains to be explored. This requires a systematic study that monitors adsorption and desorption behavior *in situ* and in real time. Quartz crystal microbalance (QCM) is one such method that measures change in mass in real time and *in situ* due to the adsorption and desorption of molecules from its surface in the form of a resonance frequency shift.[28] This is given by the Sauerbrey equation.

$$\Delta f = -\frac{2f_0^{\,2}}{A\sqrt{\mu\rho}}\Delta m \tag{1}$$

where f_0 is the resonance frequency of the uncoated QCM in air, A is the effective surface area of the electrodes, ρ and μ are the density and shear modulus of quartz, respectively.[29]

In this study, the adsorption and desorption behaviors at the urea−HA-Np interface of morphologically different HA-Np thin films are studied. Ureas have been used in medicinal chemistry for the design and optimization of various

Received: February 26, 2021
Revised: May 7, 2021

 © XXXX American Chemical Society

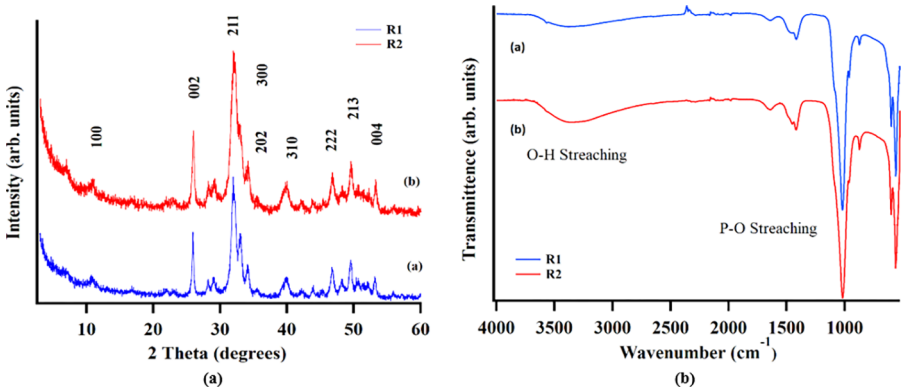

Figure 1. (a) PXRD and (b) FTIR spectra of HA-Np synthesized by route 1 (blue) and route 2 (red).

therapeutic agents.[30−37] They are also used in the field of agriculture as a nitrogen source for the plants.[19,22,23] Furthermore, urea has become an important functional group in biomolecules with a broad range of bioactivities due to its unique hydrogen bonding capabilities. In this study, urea is used as a model molecule with the view of developing a broader understanding of interactions of urea-based biomolecules.

■ MATERIALS AND METHODS

Chemicals and Materials. Urea (99% ,Sigma), ortho-phosphoric acid (H_3PO_4) (88%, Sigma), calcium hydroxide ($Ca(OH)_2$) (95%, Sigma), diammonium hydrogen phosphate ($(NH_4)_2HPO_4$) (98%, Sigma), absolute ethanol (C_2H_5OH) (99%, VWR chemicals), sulfuric acid (H_2SO_4) (97%, Sigma), hydrogen peroxide (H_2O_2) (35 wt %, Sigma), potassium hydrogen phosphate (K_2HPO_4) (98%, Sigma), and potassium dihydrogen phosphate (KH_2PO_4) (99%, Sigma) were used as received. All aqueous solutions were prepared using deionized water. Piranha solution (3:1, H_2SO_4 to H_2O_2) was used to clean glassware, reaction cells, and Au QCM crystals prior to use (Warning: Piranha solution is a strong oxidant and reacts violently with organic materials. It also presents an explosion danger. Therefore, it should be handled with caution. All work should be performed under a fume hood).

Fabrication of HA-Np on QCMs. QCM crystals (10 MHz, International Crystal Manufacturing) with 100 nm-thick vapor-deposited gold electrodes were used as the substrate in this study. Fabrication of HA-Np on QCMs was carried out as previously reported.[38] Here, HA-Nps with rod-like and bead-like morphologies were synthesized from two routes, named route 1 (R1) and route 2 (R2) and then deposited on QCM crystals. Synthesis procedure of abovementioned HA-Nps is reported in the Suporting Information. Deposition of HA-Np was carried out via spin and electrophoretic techniques to selectively obtain surfaces with (100) and (002) preferential crystal orientations. These surfaces are referred to as HA-Np(R1) and HA-Np(R2).

In summary, HA-Np suspension was prepared by ultrasonically dispersing HA-Np powder in absolute ethanol for 1 h. Spin coating and EPD techniques were used to fabricate a similar amount of HA-Nps on gold QCMs from the prepared suspension. Spin coating was carried out at 3500 rpm for 5 min using HA-Np synthesized via route 1. EDP was done using HA-Nps prepared via route 2, dispersed in ethanol, with stainless steel (316) as the anode and QCM as the cathode. These coatings were fabricated on gold by EPD at a constant voltage and time of 10 V and 6 s, respectively. Loosely bound particles were removed by ultrasonic treatment (28 kHz, 100 W) in deionized water for 5 s. Then, the coating was heat treated using a tungsten lamp for 3 h. Resonance frequency of the QCM crystal before and after the fabrication of the coating was monitored. Sauerbrey equation was used to calculate the amount of HA-Nps deposited on the QCM crystals from the measured change in frequency.

Monitoring Adsorption and Desorption of Urea. The experimental setup consists of Gamry's Quartz Crystal Microbalance-eQCM 10 M and a flow cell (ALS Co.,Ltd) connected to a computer. Data acquisition was carried out using Gamry resonator software. A peristaltic pump was used to supply the solutions at a constant flow rate. The HA-Np-coated QCM crystal was clamped in the flow cell with O-rings on both sides, resulting in only one face being exposed to the liquid with a geometric area of 0.205 cm^2. A 10 mM phosphate buffer solution (PBS, KH_2PO_4, and K_2HPO_4; pH 7.0) was pumped into the flow cell at a constant flow rate using a peristaltic pump. PBS was used as most biological reactions are conducted in PBS where the stability of HA coatings was also found to be high.

After the system had reached a frequency stability of ≤1 Hz, 1 M urea solution was sent to the flow cell using the peristaltic pump. The resonance frequency was continuously recorded after injection until it reached an equilibrium. The above procedure was repeated with 2, 3, and 4 M urea solutions, and triplicate data were obtained for each concentration. In order to monitor the desorption, PBS solution was sent through the flow cell after the adsorption of urea at each concentration until it reached a plateau, which confirmed the completion of the desorption process. All experiments were carried out at room temperature (∼32 °C). All QCM curve fittings were done using the Igor Pro software version 8.02.

Characterization. Powder X-ray diffraction (PXRD) patterns of all HA-Nps synthesized using the two routes, R1 and R2, were recorded using a Bruker D8 Focus X-ray powder diffractometer using Cu Kα radiation (λ = 0.154 nm) over a 2θ range of 3−60°, with a step time of 1 s and a step size of 0.02°.

FTIR spectra of HA-Nps synthesized using R1, HA-Nps synthesized using R2, and pure urea were obtained in ATR mode using a Thermo Scientific Nicolet IS 10 spectrometer. IR spectra with a wavenumber resolution of 1 cm^{-1} were recorded between 4000 and 600 cm^{-1}.

FTIR spectra were obtained on the surfaces of HA-Np samples and on urea adsorbed HA-Np(R1) (HA-Np(R1)-U) and urea adsorbed HA-Np(R2) (HA-Np(R2)-U) samples using a Tensor 27 Bruker Fourier transform infrared spectrometer equipped with a mercury cadmium telluride (MCT) detector, a specular reflectance accessory (VeeMaxII), and a ZnSe polarizer. Spectra were obtained at 70° incidence using p-polarized light with 256 scans at 4 cm^{-1} resolution using a bare substrate as the background. These data were obtained in triplicates to calculate the error.

X-ray photoemission spectroscopy (XPS) of HA-Np coatings was carried out using a Thermo Scientific TM ESCALAB Xi+ spectrometer in an ultrahigh vacuum chamber at 1×10^{-10} mbar of base pressure with Al Kα (1486.6 eV) as an X-ray source. Spectra were recorded with an analyzer resolution of 0.05 eV. Atomic ratios were calculated by fitting spectra with vigot function after Shirley background correction using Igor Pro 8 software.

Scanning electron microscopy (SEM) (Zeiss evo ls 15, EHT 20 KV, Mag: 100KX) was performed to study the morphology of the

https://doi.org/10.1021/acs.langmuir.1c00564
Langmuir XXXX, XXX, XXX−XXX

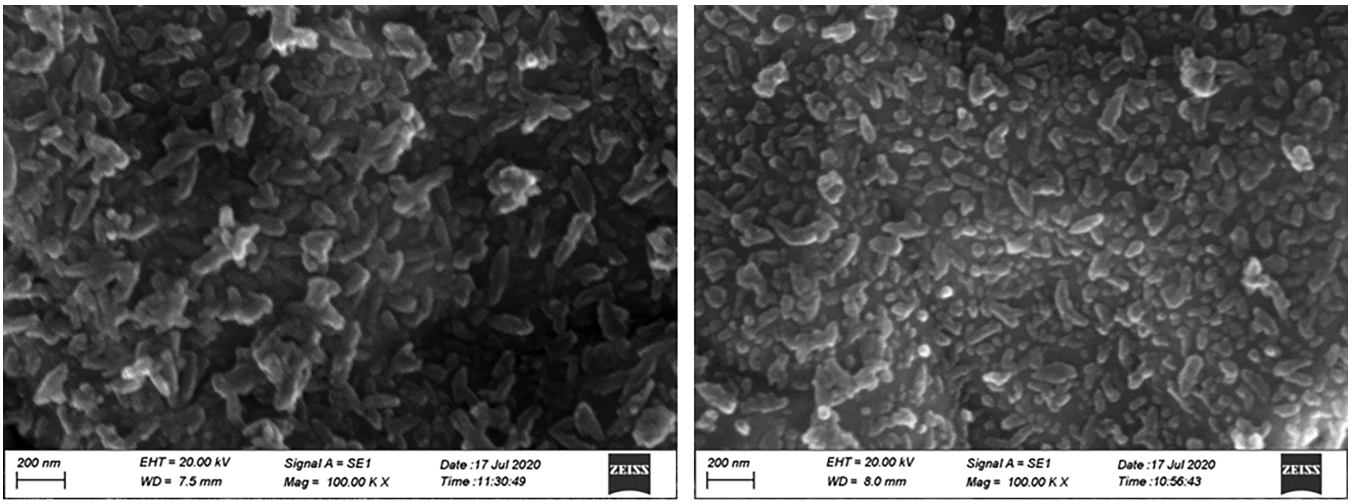

(a) (b)

Figure 2. SEM images of (a) HA-Np(R1) and (b) HA-Np(R2).

synthesized samples. A thin gold coating was applied on the samples prior to imaging.

■ RESULTS AND DISCUSSION

Hydroxyapatite, with unit cell dimensions of $a = b = 9.432$ Å and $c = 6.881$ Å, crystallizes in the space group $P63/m$. The crystal surface of the heterogeneous primitive unit cell consists of two different binding sites known as PO_4^{3-} sites and Ca^{2+} sites. PO_4^{3-}-sites are arranged hexagonally on the (a, b) crystal face, *i.e.*, (002) plane of HA, while Ca^{2+}- sites are arranged on the (a, c) or (b, c) crystal face in a rectangular manner, which is (100) plane.[39−41] The crystal structure of HA-Nps is given in the Figure S1 in the Supporting Information.

Powder X-ray diffraction (PXRD) and Fourier transform infrared spectroscopy (FTIR) methods were performed to characterize HA-Nps synthesized using R1 and R2. These spectra are shown in Figure 1 and are consistent with previously reported results.[38] The PXRD patterns shown in Figure 1a of both R1 and R2, is of a single crystalline phase. In the FTIR spectra (Figure 1b), four prominent absorbances can be seen approximately at wavenumbers 3500, 1400, 1085, and 500 cm^{-1} that is typical for HA-Nps and corresponds to O−H stretching vibrations of the hydroxyl groups, O−H−O bending vibrations of water molecules, and P−O asymmetric stretching and bending vibrations, respectively.

Figure 2 shows the scanning electron microscopy (SEM) images of HA-Np(R1) and HA-Np(R2) of which QCM measurements were made. Respectively, these samples were made by spin and EPD coating equal amounts of HA-Np prepared from R1 and R2 onto Au QCMs. The two images show different surface morphologies, rod-like (Figure 2a) and bead-like (Figure 2b), of HA-Np particles that fully cover the QCM surface. These results are indicative of the preferential crystal orientation of HA-Nps on each of these surfaces.

Figure 3 shows the FTIR spectra of both HA-Np(R1) and HA-Np(R2) surfaces. These spectra are the same as the HA-Nps of the two routes R1 and R2, as shown in Figure 1b. As mentioned above, the most prominent absorption band at 1085 cm^{-1} is attributed to the P−O symmetric stretching of PO_4^{3-} ions in HA-Nps. It is evident from the figure that HA-Np(R2) contains a higher amount of phosphates on the surface compared to that on HA-Np(R1). To further confirm the above observation, XPS spectra of P 2p and Ca 2p regions were obtained for HA-Np(R1) and HA-Np(R2) and are shown in Figure 4. Calculated peak area ratios of P 2p/Ca 2p, by fitting spectra with vigot function after Shirley background correction, were 0.55 and 1.23 for HA-Np(R1) and HA-Np(R2), respectively. These results indicate existence of more PO_4^{3-} sites in comparison to Ca^{2+} sites on the HA-Np(R2) surface. Thus, the results are consistent with previous FTIR observations.

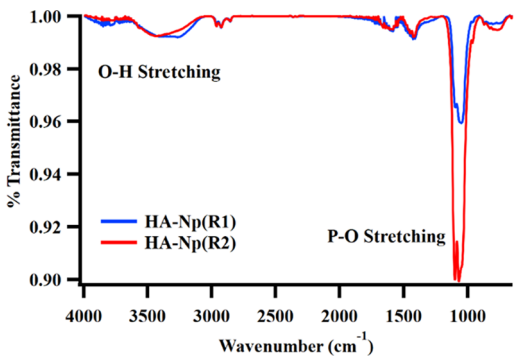

Figure 3. FTIR spectra of HA-Np(R1) (blue) and HA-Np(R2) (red) surfaces.

This study aims at understanding the influence of morphology on the adsorption and desorption kinetics of urea in PBS *in situ* and in real time and thereby obtains mechanistic details of this interfacial interaction. Figure 5a,b shows QCM frequency changes (df) obtained from adsorption and subsequent desorption of urea for HA-Np(R1) and HA-Np(R2) under dynamic flow condition for a range of urea concentrations, respectively. Both adsorption and desorption curves show the reversibility of the adsorption process for all studied concentrations of urea. Importantly, for each of the urea concentrations studied, the data shows that desorption rates are approximately 10 times slower than adsorption rates for both morphologies. Additionally, within the adsorption and desorption behaviors, significant changes can be seen for urea adsorption and desorption from HA-Np(R1) and HA-Np(R2), which are represented by blue and red lines, respectively.

https://doi.org/10.1021/acs.langmuir.1c00564
Langmuir XXXX, XXX, XXX−XXX

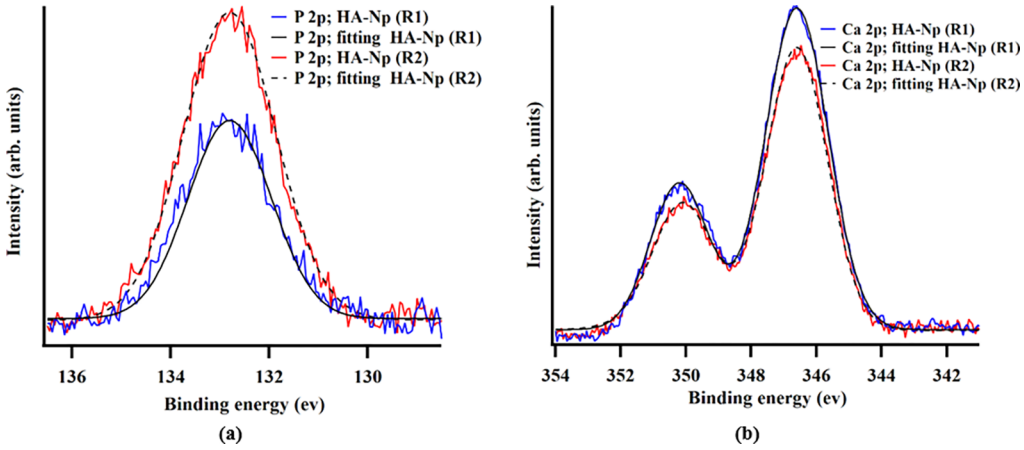

Figure 4. XPS spectra of (a) P 2p and (b) Ca 2p of HA-Np(R1) (blue) and HA-Np(R2) (red) surfaces.

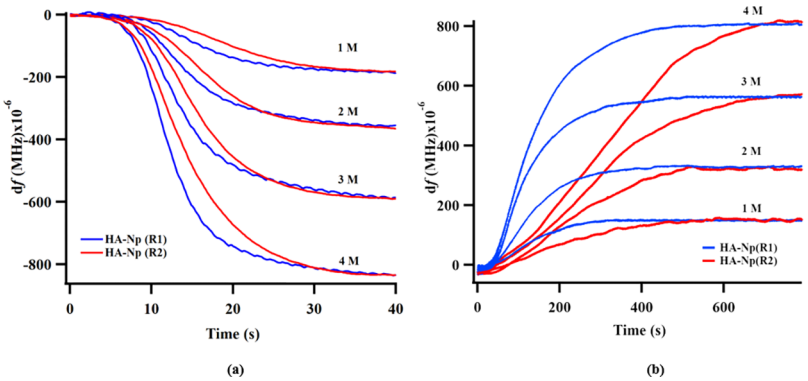

Figure 5. Urea (a) adsorption on HA-Np(R1) and HA-Np(R2) and (b) desorption from HA-Np(R1)-U and HA-Np(R2)-U for urea concentrations of 1, 2, 3, and 4 M.

Figure 5a shows urea adsorption onto HA-Np(R1) and HA-Np(R2) for a range of urea concentrations from 1 to 4 M in PBS. All curves, sigmoidal in shape, show an initial lag period and exponential adsorption followed by an asymptotic approach to equilibrium. The existence of the lag period could be explained where the dynamic equilibrium between phosphates of HA-Nps and PBS is broken for the adsorption of urea. Additionally, data shows that adsorption takes place at two different rates on the two different morphologies. However, the equilibration amount of urea adsorbed on both surfaces remains the same for its respective concentrations. For each given concentration, urea on the surface comes to a dynamic equilibrium with urea in solution. Further, the amount adsorbed at equilibrium increases with the urea concentration. The latter indicates that the HA surface is not fully saturated by urea and there remains more binding sites for urea on the HA surface.

Figure 5b presents QCM data for urea desorption into PBS from the corresponding urea adsorbed samples shown Figure 5a. For clarity, these HA-Np surfaces were refered to as HA-Np(R1)-U and HA-Np(R2)-U. Here, a more significant change can be observed in the rates of the desorption of urea from HA-Np(R1)-U and HA-Np(R2)-U in comparison to the rate deference observed during urea adsorption onto the above two respective surfaces. Additionally, from Figure 5, it is evident that urea adsorption is reversible with all adsorbed urea being subsequently desorbed during the desorption process. Furthermore, the desorption curves are sigmoidal in shape and can be attributed to an initial lag with the disintegration and disaggregation of releasing molecules followed by an exponential release through dissolution.[42]

To obtain more insight into the mechanistic details of the adsorption and desorption behavior of urea from the above two surfaces, the QCM data were fitted with sigmoidal kinetic models. This was carried out using different sigmoidal models: logistic model (LM), Weibull model (WM), and empirical Hill model (EHM).[41−45] Figure 6 shows the graphical fittings with EHM, which gives the best fit, based on the correlation coefficient, for the adsorption data presented in Figure 5a. Fittings with each of the other models can be found in Supporting Information, Figure S2.

The Hill model was first developed to explain the bonding mechanism between oxygen and hemoglobin.[46] Later, it was used to describe multivalent interactions of proteins with hydrophobic agaroses,[47] protein adsorption on hydroxyapatite,[41] and fibrilization of human Tau.[45] The EHM equation, which is used to fit QCM data, is given by

$$F(t) = F(\infty)\frac{(t/t_{50})^n}{1 + (t/t_{50})^n} \tag{2}$$

where, $F(t)$ is the frequency shift after time t of adsorption, $F(\infty)$ is the resonance frequency at saturation, t_{50} is the elapsed time at which F is equal to one half of $F(\infty)$, and n is the cooperative parameter (Hill coefficient). Generally, cooperativity is defined; positive when $n > 1.5$, partially positive when $1 < n < 1.5$, partially negative when $(0.5 < n < 1)$, and negative when $n < 0.5$.

https://doi.org/10.1021/acs.langmuir.1c00564
Langmuir XXXX, XXX, XXX−XXX

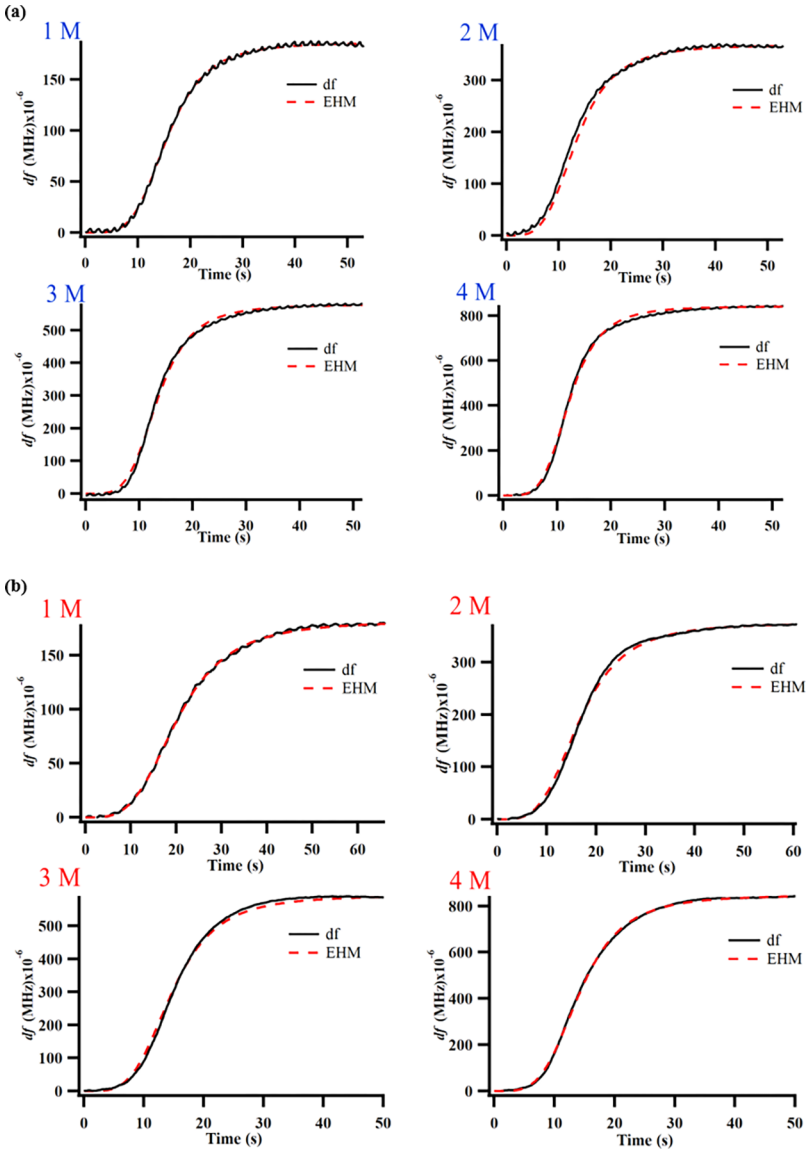

Figure 6. EHM fittings of urea adsorption on (a) HA-Np (R1) and (b) HA-Np (R2) for urea concentrations of 1, 2, 3, and 4 M.

Cooperative binding takes place if a molecule with multiple groups has an affinity for the sorbent surface, which contains multiple binding sites.[41] Hill coefficient represents the degree of cooperativity, which depends on surface concentrations of the adsorbate, nature of interactions between adsorbent and adsorbate, and lateral interactions between adsorbate molecules.[41] Moreover, cooperative binding increases with the increase in the Hill coefficient. The results from the EHM fitting for the urea adsorption data shown in Figure 6 are summarized in Table 1. It reveals that the degree of cooperativity, described by n, is greater than 1.5. This indicates positive cooperativity for adsorption of urea on both surfaces.

An increase in n with urea concentrations for both HA-Np(R1) and HA-Np(R2) is a result of the presence of more adsorbed urea on the above surfaces. Further, from Figure 5a and $F(\infty)$ values in Table 1, in both surfaces of HA-Np(R1) and HA-Np(R2), the amount of urea absorbed at equilibrium for the same concentrations of urea are equal. This reveals that the packing arrangement is approximately similar for both HA-Np surfaces at equilibrium.

Table 1. Hill Parameters n, $F(\infty)$, and t_{50} (s) of Urea Adsorption onto HA-Np(R1) and HA-Np(R2)

	n		$F(\infty)(10^{-4})$ (MHz)		t_{50} (s)	
HA-Np	(R1)	(R2)	(R1)	(R2)	(R1)	(R2)
1 M	3.850	3.711	1.922	1.872	15.65	19.87
2 M	3.982	3.811	3.603	3.654	13.35	16.21
3 M	4.160	3.892	5.826	5.952	13.27	14.53
4 M	4.281	3.990	8.351	8.350	12.45	14.13

The time at which 50% of the total amount of urea adsorbed (*i.e.*, from the amount at equilibrium) is denoted by t_{50}, which is inversely proportional to the rate of adsorption.[45,48] When considering t_{50} on both surfaces, a higher value, which denotes a lower rate of adsorption, is observed for the urea adsorption onto HA-Np(R2). Dynamic equilibrium as shown in Figure 5a is a result of adsorption and desorption. Further, it is observed that desorption rates of HA-Np(R2) are twice slower than that of HA-Np(R1). Thus, it is possible that the slower rate of adsorption is a result of the abovementioned phenomena.

https://doi.org/10.1021/acs.langmuir.1c00564
Langmuir XXXX, XXX, XXX−XXX

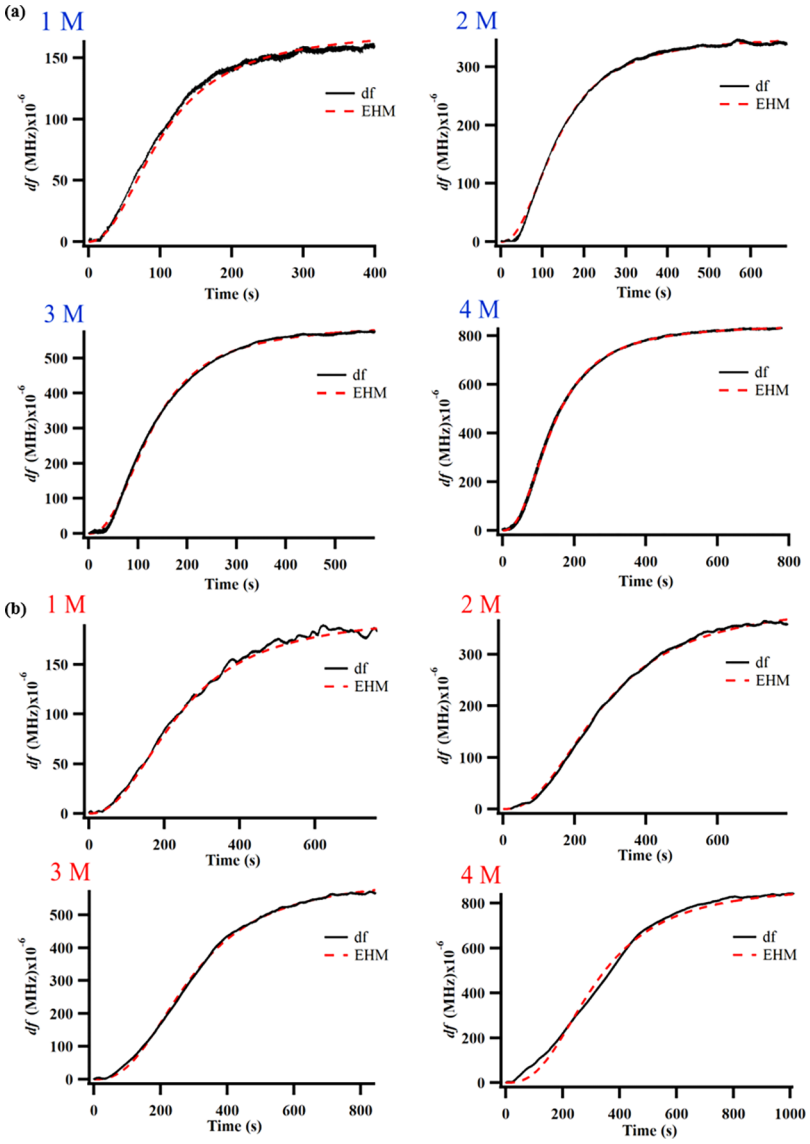

Figure 7. Fittings of urea desorption into PBS from (a) HA-Np(R1)-U and (b) HA-Np(R2)-U for urea concentrations of 1, 2, 3, and 4 M.

Additionally, as reported by us in a previous study, phosphates in the PBS are in equilibrium with phosphates on the HA-Np thin film.[38] Therefore, the results point to the likelihood that in the HA-Np(R2) surface, which is predominantly of PO_4^{3-} sites, is in dynamic equilibrium in PBS compared to the HA-Np(R1) surface prior to the adsorption of urea. Breaking this dynamic equilibrium at the PO_4^{3-} site is required for urea to bind to the HA-Np(R2) surface and thus would lead to a lower rate of adsorption at the HA-Np(R2) surface compared to the HA-Np(R1) surface.

Fittings to QCM data for the desorption of urea from HA-Np(R1)-U and HA-Np(R2)-U with the same three kinetic models above reveal that EHM gives the best fit. These fittings are shown in Figure 7 and in Supporting Information, Figure S3. Previously, the EHM has been used to study the regulation of enzyme activity[49] and modeling the release behavior of several phameceuitical drugs.[44,50−53]

Equation 2 was applied for the release study of urea from urea adsorbed HA-Np surfaces (HA-Np-U), where $F(\infty)$ is the maximum percentage of urea dissolved, and t_{50} is the release half life, the time required for 50% of the urea adsorbed on the surface, at saturation for each of the above concentrations to be released.[48]

Given in Table 2 are the fitting parameters obtained for the desorption of urea from the two different surfaces, HA-Np(R1)-U and HA-Np(R2)-U, from the EHM. The results reveal the Hill coefficient, n that represents the degree of cooperativity that is higher for HA-Np(R2)-U than that for HA-Np(R1)-U. It is reported that a higher degree of cooperativity impedes release mechanisms.[41] This suggests that the dissolution from the HA-Np(R2)-U is more difficult

Table 2. Hill Parameters of Urea Desorption into PBS from HA-Np(R1)-U and HA-Np(R2)-U

	n		$F(\infty)(10^{-4})$(MHz)		t_{50} (s)	
HA-Np	(R1)	(R2)	(R1)	(R2)	(R1)	(R2)
1 M	2.124	2.483	1.710	1.870	116.71	223.75
2 M	2.288	2.657	3.556	3.647	127.23	266.30
3 M	2.330	2.704	5.882	5.944	132.76	289.43
4 M	2.400	2.900	8.524	8.420	136.20	313.90

https://doi.org/10.1021/acs.langmuir.1c00564
Langmuir XXXX, XXX, XXX−XXX

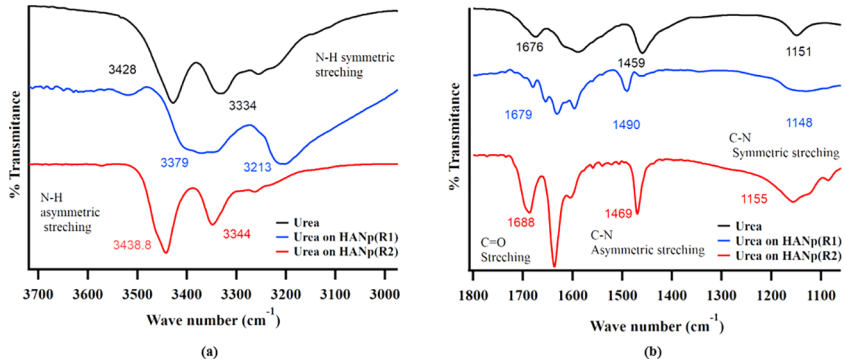

Figure 8. FTIR spectra of (black) urea, (blue) urea on HA-Np(R1), and (red) urea on HA-Np(R2) corresponding to (a) NH_2, (b) C═O, and N−C−N regions. The spectra have been shifted vertically for clarity.

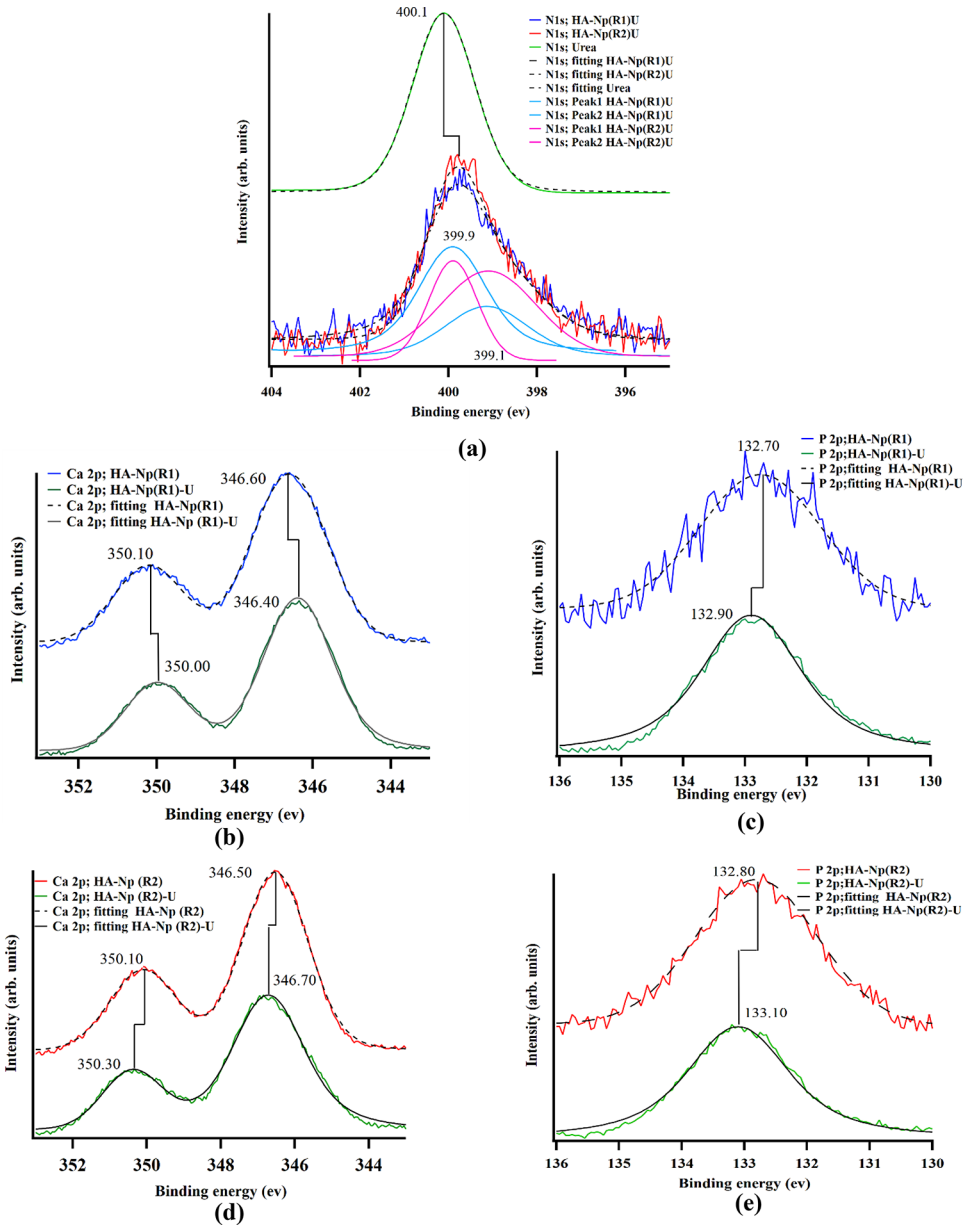

Figure 9. XPS spectra of (a) N 1s peaks of urea, HA-Np(R1)-U, and HA-Np(R2)-U. (b) Ca 2p peak of HA-Np(R1) and HA-Np(R1)-U. (c) P 2p peak of HA-Np(R1) and HA-Np(R1)-U. (d) Ca 2p peak of HA-Np(R2) and HA-Np(R2)-U. (e) P 2p peak of HA-Np(R2) and HA-Np(R2)-U. The spectra have been shifted vertically for clarity.

https://doi.org/10.1021/acs.langmuir.1c00564
Langmuir XXXX, XXX, XXX−XXX

than that from HA-Np(R1)-U. Furthermore, it indicates that urea adsorbed to the PO_4^{3-} site is released slower compared to the Ca^{2+} site The release half-life is conversely related to the release rate.[45,48] The t_{50} value HA-Np(R2)-U is approximately twice higher than that for HA-Np(R1)-U, which denotes that the release rate has decreased by half for urea desorption from HA-Np(R2)-U. This is possible where urea will have less tendency to desorb from the PO_4^{3-}-rich HA-Np(R2) to PBS, as the latter is rich in PO_4^{3-} ions.

To elucidate further the observed differences in the rates of the adsorption and desorption of urea from HA-Np(R1) and HA-Np-(R2), it is important to understand the interfacial interaction between urea and its respective HA-Np surfaces.

The nature of interactions between urea and HA-Np was studied with FTIR and XPS spectra, which are given in Figures 8 and 9, respectively.

Figure 8 shows comparative FTIR spectra of pure urea and urea bound to HA-Np(R1) and HA-Np(R2) surfaces. To obtain intensity contributions from urea adsorbed on HA-Np(R1) and HA-Np(R2), the respective HA-Np surface was used as the background during data acquisition. These IR spectra are presented in separate wavenumber regions, from 3000 to 3700 cm^{-1} (Figure 8a) and from 1000 to 1800 cm^{-1} (Figure 8b), where major IR absorbances in urea occur. IR absorbances corresponding to NH_2 asymmetric stretching, symmetric stretching, C═O stretching, N−C−N asymmetric stretching, and symmetric stretching vibrations of pure urea appear at 3428, 3334, 1676, 1459, and 1151 cm^{-1}, respectively. However, significant changes in the IR absorbance spectra can be observed in both frequency and shape of the spectra when urea is bound to HA-Np(R1) and HA-Np(R2) surfaces. This indicates the interaction of urea and HA-Np at the interface at multiple biding sites.

The above observation confirms the possibility of coorperative binding predicted by the EHM during urea adsorption onto the HA-Np surface. Also, observed in the FTIR spectra of HA-Np(R1)-U and HA-Np(R2)-U (see Supporting Information, Figure S4) is the presence of absorbance in the wavenumber region 1085 cm^{-1} corresponding to P−O stretching vibrations related to the HA-Np(R1) and HA-Np(R2) shown in Figure 1b. This confirms that the HA-Np surface is not saturated by the absorbance of urea, and more binding sites are available. This explains the reason for the observed increase in the QCM frequency shift at equilibrium with the increase in the urea concentration.

XPS analysis was carried out to further elucidate on the HA-Np and urea interaction at their respective interfaces. Figure 9 shows the XPS spectra of regions of N 1s, P 2p, and Ca 2p core level binding energies in HA-Np and HA-Np-U samples. All peaks were fitted with vigot function after Shirley background correction to obtain peak areas.

XPS spectra in the region of N 1s (Figure 9a) of HA-Np(R1)-U and HA-Np(R2)-U show similar peak areas consistent with QCM observations that show the equal amount of urea been adsorbed on both HA-Np surfaces at equilibrium. Also, it shows a shift in peak position in the N 1s core level toward lower binding energies in both HA-Np(R1)-U and HA-Np(R2)-U with respect to that of urea. Thus, it indicates the interaction between urea and HA-Np. The best fit for the XPS curve of respective HA-Np-Us' was achieved by fitting with two peaks centered at 399.9 and 399.1 eV. This is an indication of the existence of two different binding mechanisms for the two NH_2 groups of urea adsorbed on the above two surfaces.

It is possible that the higher binding energy peak (peak 1) is related to the interaction of the NH_2 group with the electron withdrawing Ca^{2+} ions, whereas the lower binding energy peak (peak 2) is related to the interaction with electron donating PO_4^{3-} ions. Calculated peak area ratios of peak 2/peak 1 of HA-Np(R1)-U and HA-Np(R2)-U are 0.58 and 1.57, respctively. Thus, indicating that more NH_2 groups are bound to PO_4^{3-} ions in HA-Np(R2)-U.

The above is confirmed with the shifts observed by the XPS spectra of Ca 2p and P 2p. Figures 9b and d show Ca 2p core level spectra for HA-Np(R1) and HA-Np(R2) and HA-Np(R1)-U and HA-Np(R2)-U, respectively. An energy shift toward the lower binding energy in the Ca 2p core level was observed after the adsorption of urea on HA-Np(R1). Meanwhile, the energy shift in Ca 2p core level for HA-Np(R2) is toward a higher binding energy. Thus, the above observation implies that the chemical environment around Ca^{2+} ions of the two HA-Np surfaces is modified differently in the presence of urea as a result of binding through different modes.

Figure 9c,e shows P 2p core level spectra for the above two types HA-Np surfaces and those of respective urea adsorbed surfaces. These spectra show peak shifts toward higher binding energies after binding to urea. Hence, this suggests that the electron density around P of HA-Np has been influenced by urea adsorption due to new interactions. However, the greater shift in the P 2p peak position of HA-Np(R2)-U compared to that of HA-Np(R1)-U indicates greater interactions between urea and HA-Nps(R2)-U.

The above details of interfacial interactions obtained by analyzing XPS, and FTIR indicates the existence of different binding modes of urea on the two HA-Np surfaces. It has been reported that the carbonyl group of urea can coordinate with metals through the C═O···metal bond and N of the amide can coordinate with metals through the N···metal bond.[54,55] Moreover, the possibility of Ca^{2+} of HA to bind with two NH_2 groups has also been reported.[56] Based on the above reported results, Figure 10 modes 1−3 show the possible bonding configurations between urea and Ca^{2+} site of HA-Nps. Furthermore, hydrogen bonding through H in the amide group with hydroxyl groups and PO_4^{3-} groups of HA-Nps is also possible (modes 4 and 5, respectively).

In Figure 8, a significant red shift can be seen in the N−H stretching vibrations for urea bound to HA-Np(R1). However, no shift in C═O stretching vibrations was observed. Thus, combined with the information from XPS analysis of HA-Np(R1) and HA-Np(R1)-U in Figure 9b, it is evident that the binding of urea to HA-Np(R1) is predominantly through N of the amide with the Ca^{2+} site via modes 2, 3, and 4.

A blue shift is observed in all of the bond vibrations identified in FTIR spectra of urea on HA-Np(R2) with respect to urea. This is in contrast to the red shift and peak broadening observed in the absorbance spectra of N−H stretching vibrations of urea bound to HA-Np(R1). This observation, together with the XPS shifts in Figure 9e, indicates that the binding of urea is predominantly through mode 5, where H of the amide binds with O of the PO_4^{3-} on the surface of HA-Np(R2). Therefore, combined XPS and FTIR results indicated the existence of different binding configurations for urea with HA-Np(R1) and HA-Np(R2). In both cases, coorperativity arise from multiple binding configurations identified by the

https://doi.org/10.1021/acs.langmuir.1c00564
Langmuir XXXX, XXX, XXX−XXX

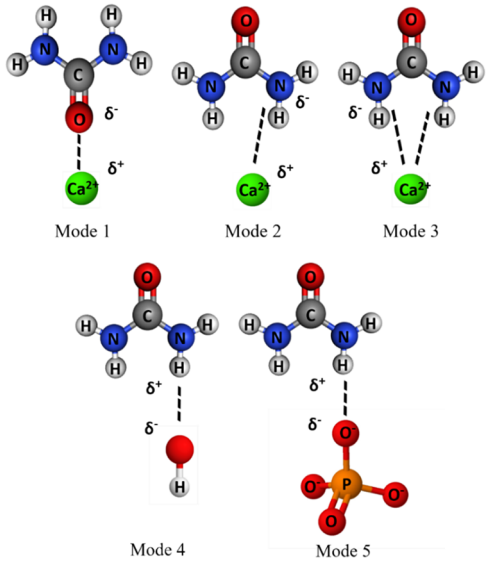

Figure 10. Urea bonding modes onto Ca^{2+} and PO_4^{3-} sites of HA-Nps.

modes in Figure 10. Moreover, both XPS and FTIR results indicate the significant interaction of urea with HA-Np(R2) compared to that with HA-Np(R1), which can be envisage as the reason for the slower release of urea observed in the QCM data for HA-Np(R2).

CONCLUSIONS

The research highlights the impact of HA-Np crystal orientation toward its interfacial kinetics with urea in the PBS. *In situ* and real-time QCM measurements show that the adsorption rate of urea onto morphologically different HA-Np surfaces, which consists predominantly of Ca^{2+} sites or PO_4^{3-} sites, differ by an order of magnitude to that of desorption rates. Moreover, the rate of the desorption of urea from the PO_4^{3-} site is half the rate of desorption from the Ca^{2+} site. It was also found that adsorption and desorption on both HA-Np sites follow the Hill kinetic model, thus indicating cooperative binding between urea and HA-Np. Moreover, combined QCM, FTIR, and XPS analyses confirm that binding mechanisms at the two morphologies are also different, thus explaining the difference in kinetics of the desorption of urea from the two surfaces of HA-Nps. Furthermore, it is evident from the observations that the morphological difference in the underline substrate affects only the rate of the adsorption and release of urea and not the amount adsorbed and the packing arrangement at equilibrium.

Importantly, the findings, for the first time, provide a mechanistic insight into the HA-Np−urea interaction and its influence on interfacial kinetics. The urea moiety is important in medicinal chemistry, and it is used as a structural motif in therapeutic drugs for the treatment of diseases such as brain tumors, metastatic prostate cancer, asthma, sickle cell anemia, and hepatitis C. This information is significant in developing HA-Np thin films with specific crystal orientation to optimize the controlled release properties of urea-based biomolecules, which have applications in bionaotechnology and nano-medicine.

ASSOCIATED CONTENT

Supporting Information

The Supporting Information is available free of charge at https://pubs.acs.org/doi/10.1021/acs.langmuir.1c00564.

Crystal structure of HA-Np (100) and (002) planes, HA-Np synthesis via R1 and R2, QCM data fittings of adsorption and desorption of urea, and FTIR of urea adsorbed on HA-Nps (PDF)

AUTHOR INFORMATION

Corresponding Author

Dilushan R. Jayasundara − *Department of Physics, University of Colombo, Colombo 00300, Sri Lanka;* orcid.org/0000-0001-9220-1130; Email: dilushanj@phys.cmb.ac.lk

Authors

Nimshi L. Fernando − *Department of Physics, University of Colombo, Colombo 00300, Sri Lanka*

Dhanusha T. N. Rathnayake − *Department of Physics, University of Colombo, Colombo 00300, Sri Lanka*

Nilwala Kottegoda − *Department of Chemistry, University of Sri Jayewardenepura, Nugegoda 10250, Sri Lanka;* orcid.org/0000-0002-9664-1704

J. K. D. Sumedha Jayanetti − *Department of Physics, University of Colombo, Colombo 00300, Sri Lanka;* orcid.org/0000-0003-4961-0902

Veranja Karunaratne − *Department of Chemistry, University of Peradeniya, Peradeniya 20400, Sri Lanka*

Complete contact information is available at: https://pubs.acs.org/10.1021/acs.langmuir.1c00564

Author Contributions

The manuscript was written through contributions of all authors. All authors have given approval to the final version of the manuscript.

Notes

The authors declare no competing financial interest.

ACKNOWLEDGMENTS

The authors gratefully acknowledge financial support of the National Research Council Sri Lanka (NRC grant 15-004). The authors would also like to acknowledge Prof. Paula Colavita, Trinity College Dublin, Prof N. V. Chandrasekharan for providing pumps for experiments, The Center for Advanced Materials Research of the University of Sri Jayewardenepura, Sri Lanka, Department of Materials Science and Engineering, University of Moratuwa, Sri Lanka, and Sri Lanka Institute of Nano Technology and Techno Solutions (pvt) Ltd., Sri Lanka for the use of their instrumentation facilities.

REFERENCES

(1) Yuan, L.; Chen, W.; Hu, J.; Zhang, J. Z.; Yang, D. Mechanistic study of the covalent loading of paclitaxel via disulfide linkers for controlled drug release. *Langmuir* **2013**, *29*, 734−743.

(2) Vázquez-González, M.; Willner, I. DNA-responsive SiO_2 nanoparticles, metal−organic frameworks, and microcapsules for controlled drug release. *Langmuir* **2018**, *34*, 14692−14710.

(3) He, D.; He, X.; Wang, K.; Zou, Z.; Yang, X.; Li, X. Remote-controlled drug release from graphene oxide-capped mesoporous silica to cancer cells by photoinduced pH-jump activation. *Langmuir* **2014**, *30*, 7182−7189.

(4) Ferraz, M.; Mateus, A.; Sousa, J.; Monteiro, F. Nano-hydroxyapatite microspheres as delivery system for antibiotics: release kinetics, antimicrobial activity, and interaction with osteoblasts. *J. Biomed. Mater. Res. A* **2007**, *81*, 994−1004.
(5) Ghosh, R.; Swart, O.; Westgate, S.; Miller, B. L.; Yates, M. Z. Antibacterial copper−hydroxyapatite composite coatings via electrochemical synthesis. *Langmuir* **2019**, *35*, 5957−5966.
(6) Katti, K. S.; Katti, D. R.; Dash, R. Synthesis and characterization of a novel chitosan/montmorillonite/hydroxyapatite nanocomposite for bone tissue engineering. *Biomed. Mater.* **2008**, *3*, No. 034122.
(7) Li, B.; Kan, L.; Zhang, X.; Li, J.; Li, R.; Gui, Q.; Qiu, D.; He, F.; Ma, N.; Wang, Y.; Wei, H. Biomimetic bone-like hydroxyapatite by mineralization on supramolecular porous fiber networks. *Langmuir* **2017**, *33*, 8493−8502.
(8) Liu, Q.; Guo, W.; Yang, M.; Wang, K.; Liu, W.; Wu, F. Release behavior of folic acid grafted hollow hydroxyapatite as drug carrier. *Adv. Polym. Technol.* **2019**, 1−9.
(9) Lobo, A. O.; Corat, M. A. F.; Ramos, S. C.; Matsushima, J. T.; Granato, A. E. C.; Pacheco-Soares, C.; Corat, E. J. Fast preparation of hydroxyapatite/superhydrophilic vertically aligned multiwalled carbon nanotube composites for bioactive application. *Langmuir* **2010**, *26*, 18308−18314.
(10) Macha, I. J.; Karacan, I.; Ben-Nissan, B.; Cazalbou, S.; Müller, W. H. Development of antimicrobial composite coatings for drug release in dental, orthopaedic and neural prostheses applications. *SN Appl. Sci.* **2018**, *1*, 68.
(11) Teixeira, J. M. C.; Alburquerque, J. S. V.; Duarte, E. B.; Silva, S. A.; Nogueira, R. E. F. Q. In vitro drug release study from hydroxyapatite-alumina composites. *J. Sol-Gel Sci. Technol.* **2019**, *89*, 521−530.
(12) Teng, S.-H.; Lee, E.-J.; Wang, P.; Jun, S.-H.; Han, C.-M.; Kim, H.-E. Functionally gradient chitosan/hydroxyapatite composite scaffolds for controlled drug release. *J. Biomed. Mater. Res., Part B* **2009**, *90B*, 275−282.
(13) Yu, F.; Wang, J.; Tong, L.; Zhang, X. Studies of a novel hydroxyapatite sustained-release preparation for temozolidomide implantation. *Mater. Chem. Phys.* **2019**, *228*, 221−227.
(14) Martins, M. L.; Pinto, T. S.; Gomes, A. M.; Parra, J. P. R. L. L.; Franchi, G. C., Jr.; Zambuzzi, W. F.; Rodrigues, C. G. Immobilization of paclitaxel on hydroxyapatite for breast cancer investigations. *Langmuir* **2020**, *36*, 8723−8732.
(15) Li, J.; Liu, M.; Qiu, Y.; Gan, Y.; Jiang, H.; Liu, B.; Wei, H.; Ma, N. Urchin-like Hydroxyapatite/Graphene Hollow Microspheres as pH-Responsive Bone Drug Carriers. *Langmuir* **2021**, *37*, 4137−4146.
(16) Liu, M.; Liu, H.; Sun, S.; Li, X.; Zhou, Y.; Hou, Z.; Lin, J. Multifunctional hydroxyapatite/Na (Y/Gd) F4: Yb3+, Er3+ composite fibers for drug delivery and dual modal imaging. *Langmuir* **2014**, *30*, 1176−1182.
(17) Montalvo, D.; McLaughlin, M. J.; Degryse, F. Efficacy of hydroxyapatite nanoparticles as phosphorus fertilizer in andisols and oxisols. *Soil Sci. Soc. Am. J.* **2015**, *79*, 551−558.
(18) Liu, R.; Lal, R. Synthetic apatite nanoparticles as a phosphorus fertilizer for soybean (*Glycine max*). *Sci. Rep.* **2015**, *4*, 5686.
(19) Elhassani, C. E.; Essamlali, Y.; Aqlil, M.; Nzenguet, A. M.; Ganetri, I.; Zahouily, M. Urea-impregnated HAP encapsulated by lignocellulosic biomass-extruded composites: A novel slow-release fertilizer. *Environ. Technol. Innovation* **2019**, *15*, 100403.
(20) Marchiol, L.; Filippi, A.; Adamiano, A.; Degli Esposti, L.; Iafisco, M.; Mattiello, A.; Petrussa, E.; Braidot, E. Influence of Hydroxyapatite Nanoparticles on Germination and Plant Metabolism of Tomato (Solanum lycopersicum L.): Preliminary Evidence. *Agronomy* **2019**, *9*, 161.
(21) Sciena, C. R.; dos Santos, M. F.; Moreira, F. K. V.; Sena Neto, A. R.; Marconcini, J. M.; Correa, D. S.; Paris, E. C. Starch: Pectin Acidic Sachets Development for Hydroxyapatite Nanoparticles Storage to Improve Phosphorus Release. *J. Polym. Environ.* **2019**, *27*, 794−802.
(22) Kottegoda, N.; Sandaruwan, C.; Priyadarshana, G.; Siriwardhana, A.; Rathnayake, U. A.; Berugoda Arachchige, D. M.; Kumarasinghe, A. R.; Dahanayake, D.; Karunaratne, V.; Amaratunga, G. A. J. Urea-Hydroxyapatite Nanohybrids for Slow Release of Nitrogen. *ACS Nano* **2017**, *11*, 1214−1221.
(23) Kottegoda, N.; Munaweera, I.; Madusanka, N.; Karunaratne, V. A green slow-release fertilizer composition based on urea-modified hydroxyapatite nanoparticles encapsulated wood. *Curr. Sci.* **2011**, *101*, 73−78.
(24) Gonzalez-McQuire, R.; Chane-Ching, J.-Y.; Vignaud, E.; Lebugle, A.; Mann, S. Synthesis and characterization of amino acid-functionalized hydroxyapatite nanorods. *J. Mater. Chem.* **2004**, *14*, 2277−2281.
(25) Li, J.; Zhu, D.; Yin, J.; Liu, Y.; Yao, F.; Yao, K. Formation of nano-hydroxyapatite crystal in situ in chitosan−pectin polyelectrolyte complex network. *Mater. Sci. Eng. C* **2010**, *30*, 795−803.
(26) Poursamar, S. A.; Rabiee, M.; Samadikuchaksaraei, A.; Tahriri, M.; Karimi, M.; Azami, M. Influence of the value of the pH on the preparation of nano hydroxyapatite polyvinyl alcohol composites. *J. Ceram. Process Res.* **2009**, *10*, 679−682.
(27) Thein-Han, W. W.; Misra, R. D. K. Biomimetic chitosan−nanohydroxyapatite composite scaffolds for bone tissue engineering. *Acta Biomater.* **2009**, *5*, 1182−1197.
(28) Jayasundara, D. R.; Cullen, R. J.; Soldi, L.; Colavita, P. E. In situ studies of the adsorption kinetics of 4-nitrobenzenediazonium salt on gold. *Langmuir* **2011**, *27*, 13029−13036.
(29) Sauerbrey, G. Verwendung von Schwingquarzen zur Wägung dünner Schichten und zur Mikrowägung. *Z. Phys.* **1959**, *155*, 206−222.
(30) Jagtap, A.; Kondekar, N.; Sadani, A.; Chern, J.-W. Ureas: Applications in Drug Design. *Curr. Med. Chem.* **2017**, *24*, 622−651.
(31) López-Muñoz, F.; Ucha-Udabe, R.; Alamo, C. The history of barbiturates a century after their clinical introduction. *Neuropsychiatr. Dis. Treat.* **2005**, *1*, 329.
(32) Batra, S.; Tusi, Z.; Madapa, S. Medicinal chemistry of ureido derivatives as anti-infectives. *Antiinfect Agents Med. Chem.* **2006**, *5*, 135−160.
(33) Li, H.-Q.; Lv, P.-C.; Yan, T.; Zhu, H.-L. Urea derivatives as anticancer agents. *Anti-Cancer Agents Med. Chem.* **2009**, *9*, 471−480.
(34) Pavić, K.; Rajić, Z.; Michnová, H.; Jampílek, J.; Perković, I.; Zorc, B. Second generation of primaquine ureas and bis-ureas as potential antimycobacterial agents. *Mol. Diversity* **2019**, *23*, 657−667.
(35) Palacios, D. S.; Meredith, E. L.; Kawanami, T.; Adams, C. M.; Chen, X.; Darsigny, V.; Palermo, M.; Baird, D.; George, E. L.; Guy, C.; Hewett, J.; Tierney, L.; Thigale, S.; Wang, L.; Weihofen, W. A. Scaffold morphing identifies 3-pyridyl azetidine ureas as inhibitors of nicotinamide phosphoribosyltransferase (NAMPT). *ACS Med. Chem. Lett.* **2019**, *10*, 1524−1529.
(36) Ito, K.; Charron, C. E.; King-Underwood, J.; Onions, S. T.; Longshaw, A. I., 1-pyrazolyl-3-(4-((2-anilinopyrimidin-4-yl) oxy) napththalen-1-yl) ureas as p38 map knase inhibitors. Google Patents: 2019.
(37) Longshaw, A. I.; Fordyce, E. A. F.; Onions, S. T.; King-Underwood, J.; Venable, J. D.; Walters, I., Pyrazolyl ureas as kinase inhibitors. Google Patents: 2019.
(38) Fernando, N. L.; Kottegoda, N.; Jayanetti, S.; Karunaratne, V.; Jayasundara, D. R. Stability of nano-hydroxyapatite thin coatings at liquid/solid interface. *Surf. Coat. Technol.* **2018**, *349*, 24−31.
(39) Kawasaki, T. Theory of chromatography of rigid molecules on hydroxyapatite columns with small loads: IV. Estimation of the adsorption energy of nucleoside polyphosphates. *J. Chromatogr. A* **1978**, *151*, 95−112.
(40) Kawasaki, T. Theory of chromatography on hydroxyapatite columns with small loads: V. determination of the adsorption energy of the ε-amino group of poly-l-lysine and the manner of adsorption of the molecule. *J. Chromatogr. A* **1978**, *157*, 7−42.
(41) Luo, Q.; Andrade, J. D. Cooperative adsorption of proteins onto hydroxyapatite. *J. Colloid Interface Sci.* **1998**, *200*, 104−113.
(42) Makoid, M.; Dufour, A.; Banakar, U. Modelling of dissolution behaviour of controlled release system. *STP Pharma Prat.* **1993**, *3*, 49−49.

https://doi.org/10.1021/acs.langmuir.1c00564
Langmuir XXXX, XXX, XXX−XXX

(43) Carrillo, M.; González, J. M. A new approach to modelling sigmoidal curves. *Technol. Forecast. Soc. Change* **2002**, *69*, 233−241.
(44) Murzin, D. Y.; Heikkilä, T. Modeling of drug dissolution kinetics with sigmoidal behavior from ordered mesoporous silica. *Chem. Eng. Commun.* **2014**, *201*, 579−592.
(45) Zhu, H.-L.; Meng, S.-R.; Fan, J.-B.; Chen, J.; Liang, Y. Fibrillization of human Tau is accelerated by exposure to lead via interaction with His-330 and His-362. *PLoS One* **2011**, *6*, No. e25020.
(46) Hill, A. V. The possible effects of the aggregation of the molecules of haemoglobin on its dissociation curves. *J. Physiol.* **1910**, *40*, 4−7.
(47) Jennissen, H. P.; Botzet, G. Protein binding to two-dimensional hydrophobic binding-site lattices: adsorption hysteresis on immobilized butyl-residues. *Int. J. Biol. Macromol.* **1979**, *1*, 171−179.
(48) Barzegar-Jalali, M.; Adibkia, K.; Valizadeh, H.; Shadbad, M. R.; Nokhodchi, A.; Omidi, Y.; Mohammadi, G.; Nezhadi, S. H.; Hasan, M. Kinetic analysis of drug release from nanoparticles. *J. Pharm. Pharm. Sci* **2008**, *11*, 167−177.
(49) Punekar, N. S., *Enzymes: catalysis, kinetics and mechanisms*; Springer: 2018, 461−492.
(50) Cheng, H. C. Application of Hill's equation for estimating area under the concentration-time curve (AUC) and use of time to AUC 90% for expressing kinetics of drug disposition. *J. Pharmacol. Toxicol. Methods* **2009**, *60*, 296−300.
(51) Eddington, N. D.; Marroum, P.; Uppoor, R.; Hussain, A.; Augsburger, L. Development and internal validation of an in vitro-in vivo correlation for a hydrophilic metoprolol tartrate extended release tablet formulation. *Pharm. Res.* **1998**, *15*, 466−473.
(52) Emami, J. In vitro - in vivo correlation: from theory to applications. *J. Pharm. Pharm. Sci.* **2006**, *9*, 169−189.
(53) Korhonen, O.; Kanerva, H.; Vidgren, M.; Urtti, A.; Ketolainen, J. Evaluation of novel starch acetate−diltiazem controlled release tablets in healthy human volunteers. *J. Controlled Release* **2004**, *95*, 515−520.
(54) Salman, M. Infrared spectroscopic investigations on the reaction products resulted from the interaction between silver (i) salts with urea at 90 oC. *Life* , *50*, 128.
(55) Ibrahim, O. B. Complexes of urea with Mn (II), Fe (III), Co (II), and Cu (II) metal ions. *Adv. Appl. Sci. Res.* **2012**, *3*, 18.
(56) Wakamura, M.; Kandori, K.; Ishikawa, T. Surface composition of calcium hydroxyapatite modified with metal ions. *Colloids Surf., A* **1998**, *142*, 107−116.

https://doi.org/10.1021/acs.langmuir.1c00564
Langmuir XXXX, XXX, XXX−XXX